

Interplay between columnar and smectic stability in suspensions of polydisperse colloidal platelets

Cite this: DOI: 10.1039/c3cp53065e

Enrique Velasco*^a and Yuri Martínez-Ratón^b

The phase behavior of a model suspension of colloidal polydisperse platelets is studied using density-functional theory. Platelets are modelled as parallel rectangular prisms of square section l^2 and height h , with length and height distributions given by different polydispersities δ_l and δ_h . The model is intended to qualitatively represent experimental colloidal platelet suspensions at high densities with a high degree of orientational ordering. We obtain the phase behavior of the model, including nematic, smectic and columnar phases and its dependence on the two polydispersities δ_l and δ_h . When $\delta_l > \delta_h$ we observe that the smectic phase stabilises first with respect to the columnar. If $\delta_h > \delta_l$ we observe the opposite behavior. Other more complicated cases occur, e.g. the smectic stabilises from the nematic first but then exists a first-order transition to the columnar phase. Our model assumes plate-rod symmetry, but the regions of stability of smectic and columnar phases are non-symmetric in the $\delta_l - \delta_h$ plane due to the different dimensionality of ordering in the two phases. Microsegregation effects, i.e. different spatial distribution for different sizes within the periodic cell, take place in both phases and, in each case, is more apparent in the variable associated with ordering.

Received 9th August 2013,
Accepted 24th October 2013

DOI: 10.1039/c3cp53065e

www.rsc.org/pccp

I. Introduction

The issue of polydispersity is crucial to understand the phase behaviour of colloidal suspensions of anisotropic particles, since shape and size polydispersities have a profound impact on the phase behavior of colloidal liquid-crystal suspensions. Near monodisperse colloids made of rod or plate-shaped particles present the usual cascade of liquid-crystal phase transitions as the total volume fraction is increased: isotropic (I)–nematic (N)–smectic/columnar (S/C)–crystal (K). However, colloidal particles can never be made truly identical in size and shape. Polydispersity gives rise to a complex phase behavior, with the presence of multiple phase coexistence between phases with different orientational and/or positional ordering.^{1–6} Coexistence gaps are usually broadened and for high polydispersities, strong demixing and fractionation are usually observed, with coexisting phases having dissimilar size/shape distributions. Also new phenomena, such as density inversion, are exclusive of polydisperse systems. In this case the more disordered phase (I) becomes denser than the N phase.⁶

Polydispersity has also a dramatic impact on the kinetic behavior of colloidal suspensions; a most remarkable effect consists of the extremely long times necessary for the system to reach thermodynamic equilibrium.⁵

Models for polydisperse fluids of anisotropic particles should produce as an output the size or shape density distribution function $\rho(\mathbf{r}, \Omega, \sigma)$, where \mathbf{r} and Ω denote the spatial and angular particle degrees of freedom, while σ refers to the set of polydisperse variables. The theoretical modelling of polydisperse fluids constitutes a complicated task due to the large number of degrees of freedom involved in the calculations. This in turn translates into a numerical implementation of the model which involves the evaluation of multiple integrals in a high-dimensional space. For this reason, theories of polydisperse systems are formulated in terms of simplified models which postulate that the excess part of the free-energy depends on a finite set of moments of the density distribution function.^{7,8} In this way the number of degrees of freedom is conveniently reduced and the problem becomes tractable. Within these models, the I–N^{9–11} or N–N¹² equilibria of length-polydisperse freely-rotating rods were calculated. Also, within the restricted-orientation approximation, the effect of polydispersity on the stability of the biaxial nematic phase in a mixture of uniaxial rods and plates^{13,14} or in a one-component fluid of biaxial board-like particles was recently studied.¹⁵ The scarce MC simulation results on polydisperse anisotropic particles confirm the high fractionation between the coexisting I and N phases of polydisperse infinitely-thin platelets.¹⁶ They also reveal the

^a Departamento de Física Teórica de la Materia Condensada, Instituto de Ciencia de Materiales Nicolás Cabrera and Condensed Matter Physics Center (IFIMAC), Universidad Autónoma de Madrid, E-28049 Madrid, Spain.

E-mail: enrique.velasco@uam.es

^b Grupo Interdisciplinar de Sistemas Complejos (GISC), Departamento de Matemáticas, Escuela Politécnica Superior, Universidad Carlos III de Madrid, Avenida de la Universidad 30, E-28911, Leganés, Madrid, Spain.

E-mail: yuri@math.uc3m.es

existence of a terminal polydispersity beyond which the S phase of length-polydisperse hard rods becomes unstable with respect to the C phase.¹⁷

Polydispersity in size crucially affects the formation of phases with spatial order, since it is difficult to accommodate the unit-cell dimension with the varying particle size. Once stabilised, colloidal suspensions made of discs or platelets tend to form a N phase which changes to a C phase as the particle volume fraction is increased. In the C phase particles stack one on top of the other to form columns that in turn arrange in a two-dimensional lattice. An increasing polydispersity in lateral size (disc diameter) tends to destabilize the C phase with respect to the N or S phases. In fact, above a certain threshold value, the C phase turns into a S phase provided the polydispersity in thickness is not too large. A large value of the latter discourages the formation of the layered S phase. In the case of suspensions of zirconium-phosphate mineral plate-like particles,¹⁸ where the particle thickness is constant but the particle diameter is polydisperse, the S phase was found to be stable. The effect of polydispersity on the phase behavior of these suspensions was recently studied from experimental and theoretical points of view.^{19–21} It would be desirable to be able to rationalise the effect of the different particle polydispersity coefficients on the phase behaviour, and to know in advance the ranges of values of the polydispersities where one can expect to find a particular phase.

In the present work we study the effect that size polydispersity has on the relative stability between the liquid-crystal phases with partial positional ordering, in particular between the S and C phases. Our goal is not to study the phase behavior of freely-rotating hard platelets, but only to assess how polydispersity affects the relative stability between the smectic and columnar phases of highly oriented polydisperse platelets. We use density-functional theory to analyse a suspension of colloidal platelets made from hard square cuboids, *i.e.* rectangular prisms of square cross section L^2 and thickness H , Fig. 1. The normal axes of the cuboids are taken to point along a common direction and rotations about this direction are not allowed, the sides of the particles being always parallel. This approximation does not appear to be too unrealistic considering that the orientational order parameter will be high close to the transition from the N phase to either the S or the C phase. Thus we assume that particles have a perfect biaxial nematic ordering and, as a consequence, phase transitions involving changes in orientational order are not represented. Therefore, we are focussing on

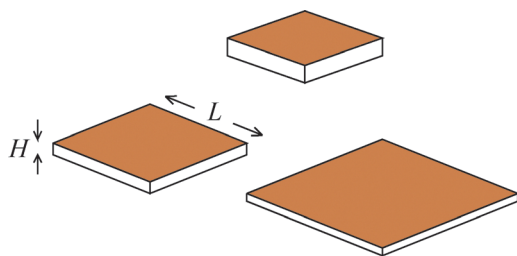


Fig. 1 Schematic of square cuboids used in this work, with particle size parameters L (side length) and H (thickness) indicated.

the stability of nonuniform (S and C) phases as compared to that of the N phase. As we will show, comparison with experiments on rods and platelet colloidal suspensions demonstrates that the effect of both polydispersities on the relative stability of S and C phases is qualitatively reproduced by our model. In real experimental samples, particles are also polydisperse in shape (having circular or polygonal square sections) and most of them exhibit a high degree of orientational order at high packing fractions, giving rise to S and/or C phases. On the other hand, computer experiments have shown that, depending on their aspect ratio, freely rotating board-like particles may form biaxial nematic, cubatic, C and S phases (the latter with or without in-plane orientational order).^{22,23} Unfortunately the study of the phase behavior of freely-rotating polydisperse particles becomes a heavy task which is outside the scope of the present work.

Our particle model can be analysed using a generalisation of the density-functional theory for hard cubes derived in ref. 24 and used for the first time to calculate the phase diagram of the one-component and binary mixture fluids.²⁵ In contrast to the latter work, where bidisperse cubes were considered, here we introduce a continuous distribution in both L and H , respectively, characterized by the distribution variances δ_l and δ_h , with a view to obtaining phase diagrams involving the N, S and C phases as a function of the two polydispersities and the particle volume fraction.

In Section II we review the density-functional theory used and give some details on the numerical methodology. Results are presented in Section III, and a short discussion and the conclusions are given in Section IV.

II. Model and numerical methodology

Density functional

The density-functional theory used is based on the fundamental-measure formalism for mixtures of parallel hard cubes. This formalism was derived by Cuesta and Martínez-Ratón,¹³ and here we generalise it to general polydisperse fluids. The excess free-energy functional in units of thermal energy $kT = \beta^{-1}$ is $\beta\mathcal{F}_{\text{ex}}[\rho] = \int_V d\mathbf{r} \Phi(\mathbf{r})$, where

$$\Phi = -n_0 \log(1 - n_3) + \frac{\mathbf{n}_1 \cdot \mathbf{n}_2}{1 - n_3} + \frac{n_{2x}n_{2y}n_{2z}}{(1 - n_3)^2}, \quad (1)$$

and where n_x are average densities,

$$n_x(\mathbf{r}) = \int_0^\infty dl \int_0^\infty dh \int_V d\mathbf{r}' \rho(\mathbf{r}'; l, h) \omega^{(\alpha)}(\mathbf{r}' - \mathbf{r}; L, H). \quad (2)$$

The index α takes the values $\{0, 1x, 1y, 1z, 2x, 2y, 2z, 3\}$. $\omega^{(\alpha)}$ are the particle geometrical measures.¹³ $\rho(\mathbf{r}; l, h)$ is the local density of particles with sizes l and h at point \mathbf{r} , where we define $l = L/L_0$ and $h = H/H_0$, with $L_0 = \langle L \rangle$ and $H_0 = \langle H \rangle$ the mean length and height, respectively. In the following we take L_0 as a unit of length, *i.e.* $L_0 = 1$. Due to the parallel particle approximation, the physics of the problem scales in the z direction, so that we can also take $H_0 = 1$. In fact, the following equivalence takes place: $\mathcal{F}[\rho; L_0, H_0]_{v_0} \equiv \mathcal{F}[\rho^*; 1, 1]$, where $\rho^*(\mathbf{r}, l, h) = \rho(\mathbf{r}, l, h)v_0$

(with $v_0 = L_0^2 H_0$ the mean volume of particle) is a local packing fraction (the difference between both free energies, coming from the ideal part, is proportional to the total number of particles and does not affect the phase behavior of the system). This scaling implies that the same functional can be used to describe a fluid of parallel platelets and a fluid of parallel rods. The equivalence will later be used to compare with different experimental results on polydisperse fluids of platelets and rods. The total free energy is then

$$\beta\mathcal{F}[\rho] = \int_0^\infty dl \int_0^\infty dh \int_V d\mathbf{r} \rho(\mathbf{r}; l, h) \{ \log[\rho(\mathbf{r}; l, h) \Lambda^3(l, h)] - 1 \} + \beta\mathcal{F}_{\text{ex}}[\rho], \quad (3)$$

which has to be minimised with respect to $\rho(\mathbf{r}; l, h)$ for each phase. $\Lambda(l, h)$ is the thermal wavelength for particles with size (l, h) , which in principle can be adsorbed into the chemical potential of that species. Here we consider the N phase, where $\rho(\mathbf{r}; l, h) = \rho(l, h)$, the S phase, with $\rho(\mathbf{r}; l, h) = \rho(\mathbf{z}; l, h)$, and the C phase, where $\rho(\mathbf{r}; l, h) = \rho(\mathbf{r}_\perp; l, h)$, and $\mathbf{r}_\perp = (x, y)$. The common particle axis is taken along \hat{z} .

An important aspect of the problem is the polydispersity of the parent solution. We can write $\rho(\mathbf{r}; l, h) = \rho_0 f(\mathbf{r}; l, h)$, where $\rho_0 = N/V$ is the total mean density, N the total number of particles, V the volume, and the function $f(\mathbf{r}; l, h)$ is the local fraction of particles of species (l, h) . It satisfies:

$$\frac{1}{V} \int_V d\mathbf{r} \int_0^\infty dl \int_0^\infty dh f(\mathbf{r}; l, h) = 1. \quad (4)$$

The global fraction is

$$x(l, h) = \frac{1}{V} \int_V d\mathbf{r} f(\mathbf{r}; l, h) = \frac{1}{N} \int_V d\mathbf{r} \rho(\mathbf{r}; l, h), \quad (5)$$

and obviously

$$\int_0^\infty dl \int_0^\infty dh x(l, h) = 1. \quad (6)$$

We assume that $x(l, h)$, the size distribution of the parent solution, is fixed and can be factorised (*i.e.* length and thickness distributions may be assumed to be uncorrelated; in the real world this may be correct or not depending on the particle synthesis methodology). Therefore we make the following assumption:

$$x(l, h) = \phi(l)\phi(h), \quad (7)$$

where $\phi(\sigma)$; $\sigma = l$ or h depending on whether one refers to the length or thickness distribution. We take

$$\phi(\sigma) = D\sigma^\gamma e^{-\lambda\sigma^2} \quad (8)$$

in terms of two parameters γ and λ . We impose the condition that the first two moments are equal to unity, which fix the

normalisation and the mean value $\langle \sigma \rangle = 1$. Then:

$$1 = \int_0^\infty d\sigma \phi(\sigma) \rightarrow D = \frac{2\lambda^{(\gamma+1)/2}}{\Gamma\left(\frac{\gamma+1}{2}\right)}, \quad (9)$$

$$1 = \int_0^\infty d\sigma \sigma \phi(\sigma) \rightarrow \lambda = \left[\frac{\Gamma\left(\frac{\gamma+2}{2}\right)}{\Gamma\left(\frac{\gamma+1}{2}\right)} \right]^2.$$

Then the second moment can be related uniquely to the polydispersity coefficient:

$$\langle \sigma^2 \rangle = \int_0^\infty d\sigma \sigma^2 \phi(\sigma) = \frac{\Gamma\left(\frac{\gamma+1}{2}\right)\Gamma\left(\frac{\gamma+3}{2}\right)}{\Gamma\left(\frac{\gamma+2}{2}\right)^2}, \quad (10)$$

and the polydispersity coefficient δ is:

$$\delta^2 = \frac{\langle \sigma^2 \rangle - \langle \sigma \rangle^2}{\langle \sigma \rangle^2} = \langle \sigma^2 \rangle - 1. \quad (11)$$

From here, the γ parameter can be obtained given an input value for δ . The equation must be solved numerically. Note that, once we fix the values of δ_l and δ_h , the values of γ_l and γ_h are in general different.

Using the free-energy functional eqn (3), the equilibrium condition reads:

$$\beta\mu(l, h) = \frac{\delta\beta\mathcal{F}}{\delta\rho(\mathbf{r}; l, h)} = \log[\rho(\mathbf{r}; l, h)\Lambda^3(l, h)] - c^{(1)}(\mathbf{r}; l, h), \quad (12)$$

$$\rightarrow \rho(\mathbf{r}; l, h) = e^{\beta\mu^*(l, h)} e^{c^{(1)}(\mathbf{r}; l, h)},$$

where $\mu(l, h)$ is the chemical potential of the species (l, h) , with

$$\mu^*(l, h) = \mu(l, h) - 3 \log \Lambda(l, h), \quad (13)$$

and $c^{(1)}(\mathbf{r}; l, h)$ the one-body direct correlation function. Integrating eqn (12) and eliminating $\mu^*(l, h)$, the Euler-Lagrange equation to be solved is:

$$f(\mathbf{r}; l, h) = x(l, h) \frac{e^{c^{(1)}(\mathbf{r}; l, h)}}{\frac{1}{V} \int_V d\mathbf{r} e^{c^{(1)}(\mathbf{r}; l, h)}}. \quad (14)$$

We define the moments

$$m_{\lambda\eta}(\mathbf{r}) = \int_0^\infty d\lambda \int_0^\infty d\eta h^\lambda h^\eta f(\mathbf{r}; l, h). \quad (15)$$

Multiplying eqn (14) by $l^\lambda h^\eta$, where λ, η are integers, and integrating over all possible values of l and h :

$$m_{\lambda\eta}(\mathbf{r}) = \int_0^\infty d\lambda \int_0^\infty d\eta h^\lambda h^\eta x(l, h) \left[\frac{e^{c^{(1)}(\mathbf{r}; l, h)}}{\frac{1}{V} \int_V d\mathbf{r} e^{c^{(1)}(\mathbf{r}; l, h)}} \right]. \quad (16)$$

If we can express $c^{(1)}$ in terms of the moments, eqn (16) form a closed set of equations for the moments.

Since there is no dependence on spatial coordinates in the N phase, eqn (1)–(3) can be used directly to evaluate the free energy.

In the case of S and C phases, we will deal with the spatial dependence by using Fourier representations. Because of the particular mathematical structure of the density functional, the one-body direct correlation function can be expressed in terms of the average densities $n_x(\mathbf{r})$ only. Therefore it is possible to use Fourier expansions for these local densities and reconstruct the local fraction of particles $f(\mathbf{r}; l, h)$ using eqn (14) evaluated at the equilibrium average densities. In the S phase, the unknown coefficients will be $c_x^{(k)}$, with

$$n_x(z) = \rho_0 \sum_{k=0}^{\infty} c_x^{(k)} \cos(qkz), \quad (17)$$

and $q = 2\pi/d$ the wavevector associated with the S period d . In the C phase, the unknown coefficients will be $\gamma_x^{(nm)}$, with

$$n_x(\mathbf{r}_{\perp}) = \rho_0 \sum_{n,m=0}^{\infty} \gamma_x^{(nm)} \cos(qnx) \cos(qmy), \quad (18)$$

where $q = 2\pi/a$ and a the lattice parameter of the square lattice. The Fourier expansions in eqn (17) and (18) were truncated so that the absolute value of the highest-order coefficient included was less than 10^{-6} for all the densities explored. In each case the Euler–Lagrange equation is solved by iterations until convergence of the coefficients. Appendix A provides more details on the numerical methodology.

A first picture of the order in which the different phases appear is provided by a bifurcation analysis. Here one perturbs the N phase with a small-amplitude density wave of given wavevector \mathbf{q} and searches for instability with respect to density and wavelength. Instability is given by the curvature of the free-energy functional, expressed by the direct correlation functional $c^{(2)}(\mathbf{r}, \mathbf{r}', l, l', h, h') = -\beta \delta^2 \mathcal{F}_{\text{ex}}[\rho] / \delta \rho(\mathbf{r}, l, h) \delta \rho(\mathbf{r}', l', h')$. The bifurcation point (density at which N becomes unstable with respect to S- or C-like perturbations) coincides with the transition point whenever the true phase transition is continuous; otherwise the bifurcation point only provides the spinodal

point and a full treatment based on equality of pressure and partial chemical potentials is needed. We provide details on the bifurcation analysis in Appendix B.

III. Results

To explore the overall structure of phase behaviour, we have first computed the bifurcation densities, *i.e.* the densities at which the Euler–Lagrange equations have a spatially inhomogeneous solution (bifurcation from the N to the S or C phases). In the following we will use the packing fraction η , defined by $\eta = \rho_0 \langle L^2 \rangle \langle H \rangle = \rho_0 (1 + \delta_l^2)$, as the relevant density parameter. Fig. 2 shows the bifurcation packing fractions η for the S and C phases as a function of one of the polydispersities when the other polydispersity is set to zero.

In the case of bifurcation to the S phase, panel (a), we see that, when $\delta_l = 0$ (dashed curve) and the thickness polydispersity δ_h increases, the packing fraction also does due to the increasing difficulty to create uniform layers in the system. The decrease in η at large values of δ_h is a microsegregation effect. Here the thickness distribution of particles is different in the layers and in between the layers (interstitials); in the former, the thickness distribution is peaked at a larger value of thickness than in the interstitials. We will comment on this effect later. The opposite case is when $\delta_h = 0$ (continuous curve). Here, as δ_l increases, the S bifurcates at lower packing fractions since platelets can better pack in the (quasi two-dimensional) layers when their side-length distribution is wider.

The bifurcation to the C phase, Fig. 2(b), is relatively similar to the S case, except that the roles of l and h are interchanged. The most notable difference is that the maximum in η does not exist, although there could also be a microsegregation effect where small platelets are expelled from the nodes of the columns to the interstitial space, as discussed later.

The overall effect of polydispersities can be visualised in the plot of Fig. 3, where the difference in bifurcation packing

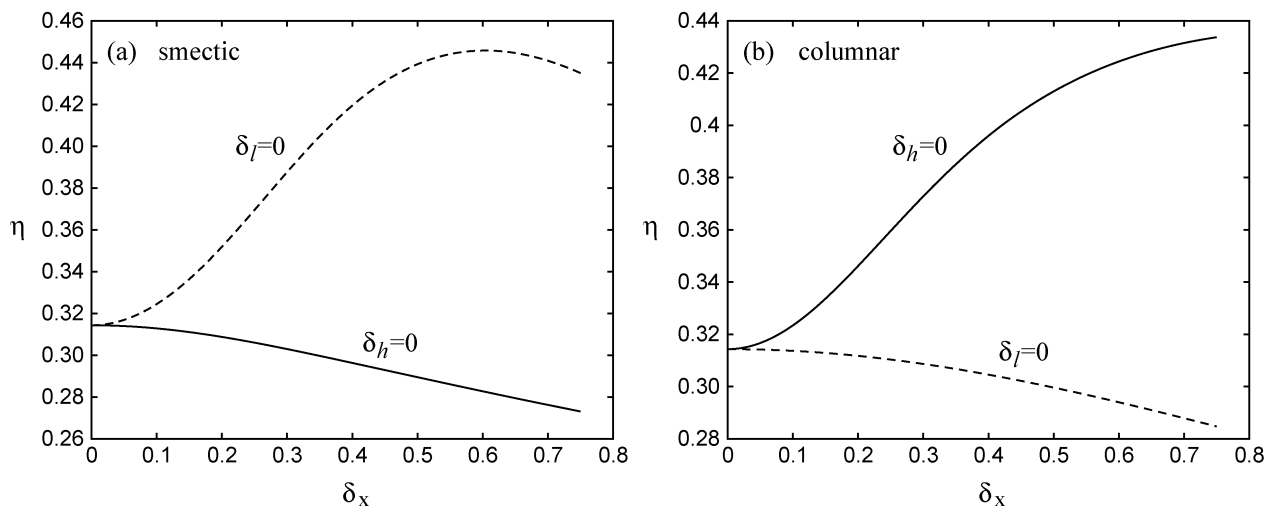


Fig. 2 Packing fractions η at which the N phase bifurcates into the (a) S, (b) C phases, as a function of one of the polydispersities δ_x ($x = l, h$) when the other polydispersity is set to zero. In both panels the continuous curve corresponds to the case $\delta_h = 0$, while the dashed curve pertains to the case $\delta_l = 0$.

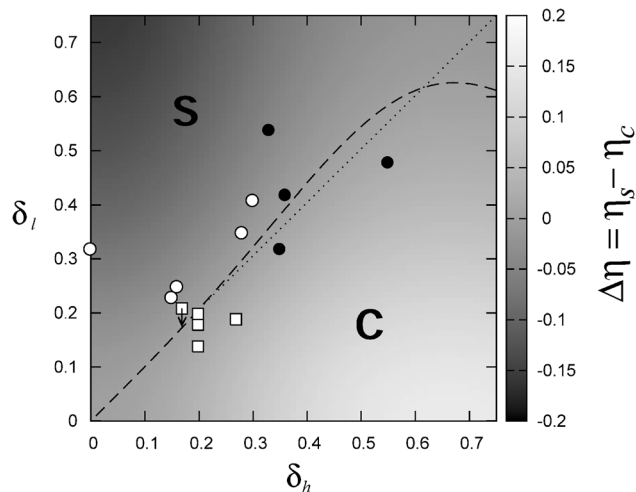


Fig. 3 Difference $\Delta\eta = \eta_s - \eta_c$ between the packing fractions of the bifurcated S and C phases as a function of polydispersity coefficients δ_l and δ_h , on a gray scale. The dashed line corresponds to the curve $\Delta\eta = 0$ where the S and C phases bifurcate at the same value of packing fraction. The S (C) label indicates the region where the S (C) phase bifurcates from the N first. Dotted line is the bisectrice $\delta_l = \delta_h$. Open squares, open circles and black filled circles correspond to experimental values of polydispersities where C, S and C + S were found. In the case of black circles and the open square with a down arrow, polydispersities correspond to those of the parent phase.

fractions $\Delta\eta = \eta_s - \eta_c$ for the S, η_s , and C, η_c , phases is shown as a function of the polydispersity coefficients δ_l and δ_h . The curve $\Delta\eta = 0$ indicates a situation where both phases bifurcate at the same packing fraction (projected black dashed curve in the figure). We see that, for large values of δ_l and δ_h , this curve does not correspond or is close to the bisectrice $\delta_l = \delta_h$ (the dotted black curve). This means that the C phase stands a higher value for its associated polydispersity coefficient (δ_l) than does the S (δ_h) up to $\delta_h \approx 0.6$; for higher values, the scenario is the opposite.

A more detailed treatment of the problem requires a full analysis beyond linear bifurcation theory, *i.e.* a full solution to the Euler-Lagrange equation (14). This allows us to obtain the free energy and the local density distribution of the different phases. Fig. 4 shows some representative cases. In this series of graphs we are following the line $\delta_l + \delta_h = 0.4$ in the $\delta_l - \delta_h$ plane. The reference case is a completely monodisperse solution, $(\delta_l, \delta_h) = (0.0, 0.0)$, for which S and C phases bifurcate at the same density, but the C phase is always more stable. Panel (a) refers to the case $(\delta_l, \delta_h) = (0.15, 0.25)$. Here the C phase bifurcates before the S, and is much more stable than the S; this is because the thickness polydispersity is relatively high and prevents the formation of regular layers. As δ_l increases and δ_h decreases, the stability gap between the two phases decreases, panels (b) and (c), and for the case (0.25, 0.15) the S phase is already more stable and bifurcates before the C phase. All of these results corroborate the results of the bifurcation analysis presented before, in the sense that a high polydispersity in one parameter (δ_l or δ_h) inhibits the formation of the corresponding phase (C or S, respectively). They also point to the fact that the δ_l and δ_h parameters do not play a

symmetric role: the C phase stands a higher value of polydispersity in its associated polydispersity than the S, and when $\delta_l = \delta_h$ the C phase is more stable than the S phase.

Note that there are some cases where the S phase bifurcates before and remains more stable than the C phase but only below some density [this occurs for values between those of panels (b) and (c)]; at higher densities the two branches should cross each other and the C phase becomes more stable (the phase transition between the two phases is of first order although no attempt has been made to calculate the properties of the coexisting phases).

The structure of the S and C phases is also interesting to investigate due to the fact that we expect strong microsegregation effects in these phases caused by the spatial ordering. By this we mean that the particle size distribution will depend on the location within the periodic unit cell. To better visualise the microsegregation effect occurring at the scale of the periodic unit cell in the S phase, we define the functions

$$h_h(z, h) = \frac{\int_0^\infty dl f(z, l, h)}{\int_0^\infty dl \int_0^\infty dh f(z, l, h)}, \quad (19)$$

$$h_l(z, l) = \frac{\int_0^\infty dh f(z, l, h)}{\int_0^\infty dl \int_0^\infty dh f(z, l, h)}.$$

$h_h(z, h)$ and $h_l(z, l)$ give, respectively, the particle thickness h distribution at point z irrespective of the side-length l and the particle side-length distribution at the same point irrespective of the thickness h . These functions for the case $\delta_l = 0.20$, $\delta_h = 0.20$ at the points located at the smectic layers (L in the figure) and at the interstitial point (I , midway between two consecutive layers) are plotted in Fig. 5(a) and (b). We can see that the first is mostly populated by the thickest particles, while the interstitial (where anyway the density of particles is much lower) mostly contains the thinner ones and the distribution is a bit broader. The effect is more important in the function associated with the ordering, *i.e.* in $h_h(z, h)$, than in the function perpendicular to it, $h_l(z, l)$. Also plotted in both figures is the global size distribution function (continuous line in grey); departure of the local functions from the global distribution gives a measure of the microsegregation effect.

As for the columnar phase, to quantify the microsegregation effect occurring at the scale of the periodic unit cell, we define the functions

$$h_l(\mathbf{r}_\perp, l) = \frac{\int_0^\infty dh f(\mathbf{r}_\perp, l, h)}{\int_0^\infty dl \int_0^\infty dh f(\mathbf{r}_\perp, l, h)}, \quad (20)$$

$$h_h(\mathbf{r}_\perp, h) = \frac{\int_0^\infty dl f(\mathbf{r}_\perp, l, h)}{\int_0^\infty dl \int_0^\infty dh f(\mathbf{r}_\perp, l, h)},$$

which again give the particle distributions at point \mathbf{r}_\perp in each polydispersity variable. In Fig. 5(c) and (d) we illustrate the microsegregation effect by plotting the distributions $h_l(\mathbf{r}_\perp, l)$ and $h_h(\mathbf{r}_\perp, h)$ at three points of the square-lattice unit cell: P , at the nodes; R , at the interstitials; and Q , midway between two nearest-neighbour nodes. The curves indicate that particles with a larger side-length tend to occupy the nodes, while small

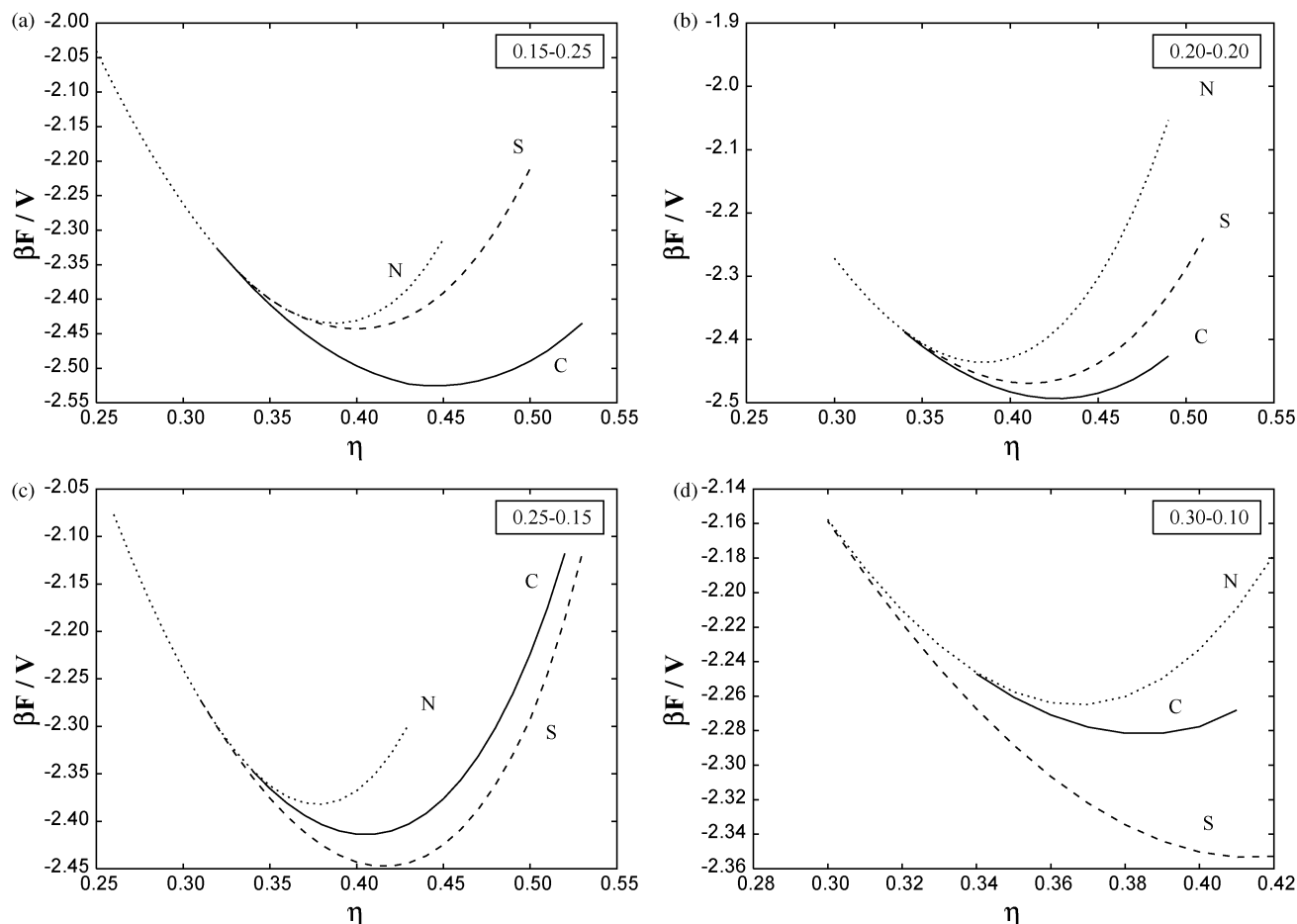


Fig. 4 Free-energy density per unit of thermal energy, $\beta F/V$, as a function of platelet packing fraction η , for different values of the polydispersities (δ_n, δ_t) . A term -8η has been added in all cases to better compare the different curves. (a) (0.15, 0.25), (b) (0.20, 0.20), (c) (0.25, 0.15) and (d) (0.30, 0.10). Free-energy branches for N, S and C phases are represented by dotted, dashed and continuous curves, respectively, and labelled by the corresponding symbol.

particles are more probable in the interstitials (where anyway the local density of particles is small). Again the microsegregation effect is more pronounced in the function associated with the ordering, in this case $h_i(\mathbf{r}_\perp, l)$, while the functions in h show a minor departure from the global distribution.

Up to now there have appeared in the literature a number of well-controlled experiments on suspensions of colloidal platelets. There are two problems when comparing the theory with the experiment. One is that polydispersities are difficult to measure with precision, especially the polydispersity in thickness. Normally one assumes that δ_n is some positive and constant value (particle synthesis normally involves exfoliation and the thickness usually consists of one or a few sheets of the original layered material), subject to large error, while δ_t is measured much more accurately and can be finely tuned more easily. The other is that suspensions are subject to gravity and the effect of sedimentation and the phase profile is crucial to understand the true phase behaviour of the suspension.²⁶ Usually this effect is not properly taken into account.

A number of groups have obtained suspensions made of particles with interactions that can be approximated as hard interactions. The Dutch group have been profusely investigating

suspensions of gibbsite particles with different polydispersities δ_i . Their δ_n is quite large and somewhat uncontrolled, so that their suspensions usually exhibit a N-to-C transition. On the other hand, the A&M Texas group has been synthesising mineral platelets with $\delta_n = 0$ (although the interactions may not always be considered as hard); in these systems the tendency to form S phases is quite strong. In a recent paper, the latter group has provided quantitative data for polydispersity in δ_t for their samples.¹⁸

In Fig. 3 some of the above experimental results on colloidal suspensions of mineral particles have been added, specially those that are relevant to elucidate the relative stability of the C and S phases. Whenever available, we plot the polydispersity coefficients (δ_n, δ_t) as measured in the fractionated coexisting phases; note that in some experiments the (in general different) polydispersities of the two coexisting phases are not measured, but only the parent or global polydispersities. In the figure, open squares show the values of the coefficients corresponding to experiments on gibbsite platelet suspensions where stable C,¹ hexatic C³⁰ and hexagonal C³¹ phases were found. The arrow pointing down in one of the open squares means that the values of (δ_n, δ_t) correspond to the parent phase. We expect that, after fractionation, δ_t will decrease. Black points correspond to

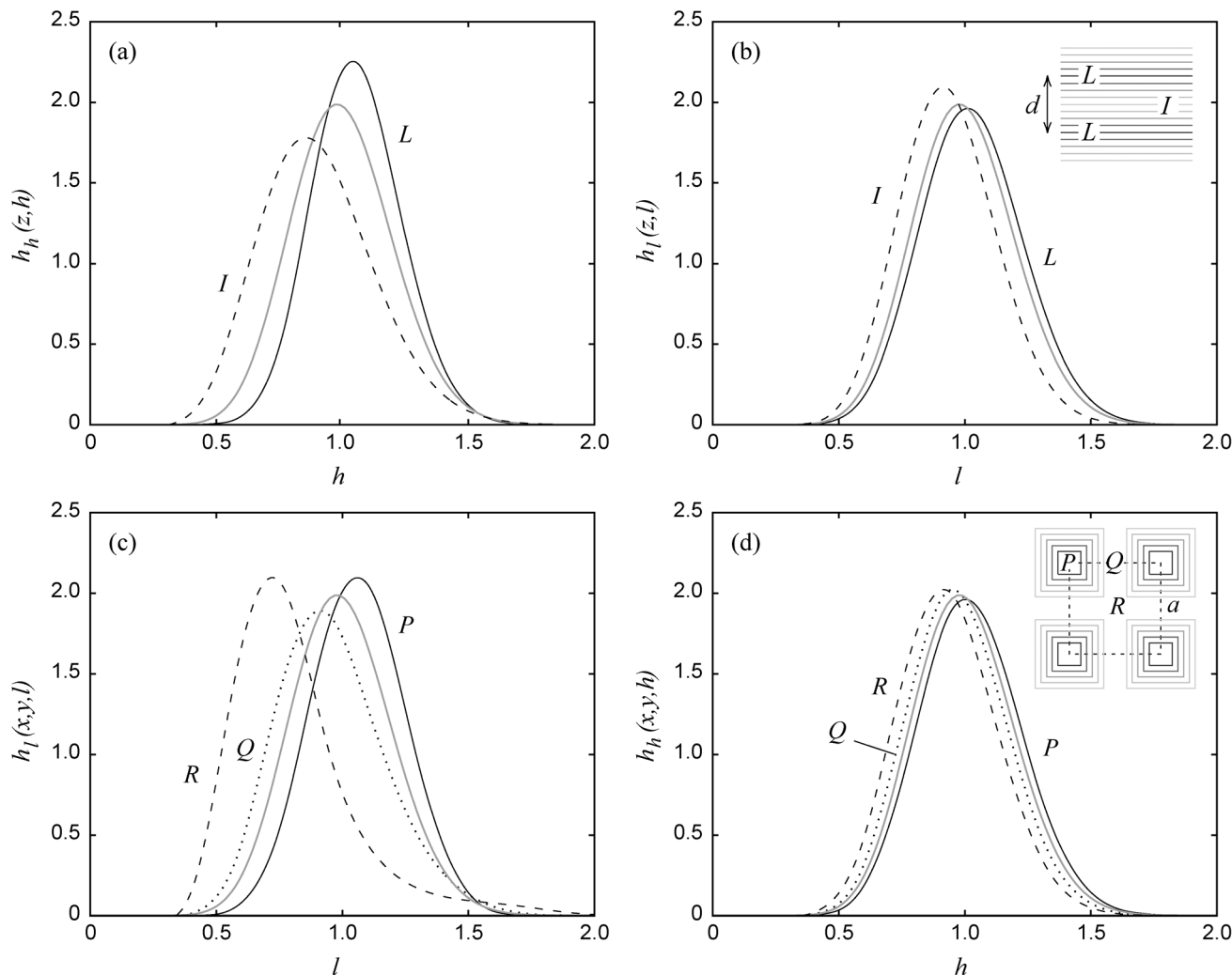


Fig. 5 The functions defined in eqn (19) and (20) for smectic and columnar phases, respectively. In all cases $\delta_l = 0.20$, $\delta_n = 0.20$ and $\eta = 0.40$. (a) and (b) smectic phase. (c) and (d) columnar phase. The smectic period d and columnar lattice parameter a correspond to the equilibrium configuration. The functions are evaluated at special points in the periodic unit cell: L (layer, $z = 0$) and I (interstitial, $z = d/2$, i.e. half smectic period) for the smectic phase and P (lattice site), Q (midway between nearest-neighbour sites) and R (interstitial site); schematic of the location of these points is included as an inset in panels (b) and (d). For reference, the global size distribution $x(l, h)$ is plotted as a continuous grey curve.

polydispersities of the parent distribution for suspensions of goethite nanorods,^{29,32} which phase separate into C and S phases. Finally, open circles with $\delta_h \neq 0$ represent values for which stable S^{29} or smectic B^{33} phases were found in suspensions of goethite nanorods²⁹ or of charged colloidal gibbsite platelets.³³ The open circle with $\delta_h = 0$ is a result from recent experiments on zirconium-phosphate mineral platelet suspensions of constant thickness but polydisperse in diameter.¹⁸ As can be seen, the values of (δ_n, δ_l) corresponding to colloidal suspensions where the C or S phases were found to be stable are approximately located in their regions predicted by our stability calculations.

IV. Conclusions

In this paper we have investigated the effect of the thickness and width polydispersities on the relative stability between the

S and C phases in a system of aligned board-like uniaxial particles, using a density-functional theory for hard cubes extended to a polydisperse mixture. An understanding of the effect of polydispersity begins with the phase behaviour of the corresponding one-component (monodisperse) system. At high densities, the system is in a K phase but the free-energy difference with the C phase is very small.^{27,28} The S phase is much less stable. All phases bifurcate from the same point (the corresponding packing fraction being $\eta = 0.3143$). Upon inclusion of polydispersity in both particle thickness and width, the K phase is expected to destabilise more strongly because the three-dimensional periodic arrangement of particles in the unit cell is very sensitive to the increase of polydispersity as compared to the higher-symmetry C and S phases. This is the reason why we have not included the K phase in the present study.

We have modelled the polydispersities in a symmetric way: the mean thickness and side length are fixed to unity, and the

global size distribution is a product of two independent functions which have the same functional form in their respective size variable. Therefore the mean particle geometry is cubic and the addition of both polydispersities deforms the original geometry to be prolate or oblate as the side length and thickness polydispersity coefficients δ_l and δ_h become nonzero. We have made a bifurcation analysis to study the effect of polydispersity on the S and C bifurcation from the N phase. The difference $\Delta\eta = \eta_s - \eta_c$ between bifurcation packing fractions allowed us to conclude that, in a first approximation, for relatively low values of δ_l and δ_h and for $\delta_l > \delta_h$ the S phase destabilizes with respect to the N phase first, while the C phase destabilizes first when $\delta_l < \delta_h$. The curve $\Delta\eta = 0$ in the $\delta_l - \delta_h$ plane is located close to the bisectrice for $\delta_h < 0.6$ (but slightly favouring the stability of the C phase), a result due to the symmetric way in which particle polydispersities are included. However, for $\delta_h > 0.6$, the curve $\Delta\eta$ deviates from the bisectrice and favours the S phase. A possible explanation for this lies in the microfractionation mechanism: for large polydispersities larger particles tend to occupy the sites of the periodic lattice (whether one dimensional in the case of the S phase or two-dimensional for the C phase) and small particles tend to occupy the lattice interstitials; this mechanism may be more effective in the S phase than in the C phase. In fact, experiments show¹ that the C phase accepts a polydispersity of at least $\delta_l = 0.25$, but recent studies on length-polydisperse rods of goethite²⁹ indicate that the S phase is stable for polydispersities as large as $\delta_h = 0.55$ (with due allowance for macrofractionation mechanisms which reduce the polydispersity of the parent sample).

The bifurcation analysis does not give the final answer to the question of relative phase behavior. To have a more profound understanding of the phase diagram of the present system and investigate the microsegregation effects, we have performed numerical minimizations of the free-energy density functional of our polydisperse fluid, fixing the probability size distribution of the parent phase $x(l, h)$ (which coincides with the unit-cell distribution in a periodic phase). We have found that, in general, the bifurcation analysis gives the correct relative stability of the C and S phases. However, there are some values of polydispersities around the $\delta_l = \delta_h$ bisectrice for which the S phase bifurcates from the N before the C phase, but at some value of packing fraction the C and S free-energy branches cross, the C phase becoming energetically favoured at higher packing fractions.

This behaviour is a clear indication that the system should exhibit a first order S–C transition. To correctly predict the particle composition of the coexisting phases, cloud-shadow coexistence calculations should be performed in which the coexistence size distributions $x_{c,s}(l, h)$ are calculated from equations expressing the equality of chemical potentials of all species and the pressures, together with the level rule (conservation of the number of particles).⁸ These calculations imply a heavy numerical task since the moments of the coexisting distributions involve the evaluation of multiple integrals and many non-linear integral equations have to be solved. Therefore, in the present paper we restricted our effort to the calculation of free-energy branches.

Finally, to confirm the microsegregation scenario, we examined the actual structure of the phases and the spatial distribution of species with different sizes. In effect, the layers or sites are preferentially populated by big particles, while the interstitials have a higher proportion of small particles. Particles with intermediate sizes have a similar composition in both locations, indicating their relatively high diffusivity. In both phases the microsegregation effect is more apparent in the polydispersity variable associated with ordering (l in the columnar phase and h in the smectic phase). For high polydispersities, the two degrees of freedom associated with size conspire with the different dimensionality of ordering in the two phases (one or two in the S and C phases, respectively) to give a non-symmetric stability map in a fluid of our otherwise perfectly symmetric particles.

The present idealized model have been used as a tool to qualitatively study the effect of size polydispersity on the stabilization of phases with partial spatial ordering (specifically the S and C phases), once the degree of orientation order is saturated at high densities. It would be interesting to study the effect of both polydispersities on the phase transitions between phases with different orientational symmetries such as isotropic, nematic, biaxial nematic and cubatic phases, which have been found in recent simulation work on board-like particles.^{22,23} By construction our model cannot be applied for this purpose. We leave this study as a future line of research.

Appendix A: numerical details

Here we give more details about the way we performed the numerical calculations.

Smectic phase

The Euler–Lagrange equation for the local fraction of particles is

$$f(z; l, h) = \frac{x(l, h)e^{\Delta c^{(1)}(z; l, h)}}{\int_0^d dz' e^{\Delta c^{(1)}(z'; l, h)}}, \quad (\text{A1})$$

where d is the S period, and $\Delta c^{(1)}(z; l, h) = c^{(1)}(z; l, h) - c_0^{(1)}(l, h)$, with $c_0^{(1)}(l, h)$ the excess part of the chemical potential (in thermal units KT) or bulk one-body direct correlation function (this is done to improve numerical accuracy). Now we expand in Fourier space:

$$f(z; l, h) = \sum_{k=0}^{\infty} f_k(l, h) \cos(kqz), \quad (\text{A2})$$

where $q = 2\pi/d$ and $f_0(l, h) = 1$. Multiplying eqn (A1) by a cosine function and integrating over one period, we obtain

$$f_k(l, h) = 2x(l, h) \frac{\int_0^d dz e^{\Delta c^{(1)}(z; l, h)} \cos(kqz)}{\int_0^d dz e^{\Delta c^{(1)}(z; l, h)}}, \quad (\text{A3})$$

with $k > 0$. Now using the definitions

$$\begin{aligned} c_{rs}^{(k)} &\equiv \int_0^\infty dl l^r \int_0^\infty dh h^s f_k(l, h) \cos\left(\frac{kqh}{2}\right), \\ s_{rs}^{(k)} &\equiv \frac{2}{kq} \int_0^\infty dl l^r \int_0^\infty dh h^s f_k(l, h) \sin\left(\frac{kqh}{2}\right), \end{aligned} \quad (\text{A4})$$

with $r, s = 0, 1, \dots$, the corresponding projections of the Euler-Lagrange equations, given by eqn (A3), can be rewritten solely in terms of the $\{c_{rs}^{(k)}, s_{rs}^{(k)}\}$ coefficients. This is because, as can be easily shown, the average functions n_x depend on these coefficients only:

$$n_x(z) = \rho_0 \sum_{k=0}^\infty d_x^{(k)} \cos(qkz), \quad (\text{25})$$

where, for each value of $k > 0$,

$$d_x = \{c_{00}, c_{10}, c_{10}, s_{00}, s_{10}, s_{10}, c_{20}, s_{20}\} \quad (\text{A6})$$

for $\alpha = \{0, 1x, 1y, 1z, 2x, 2y, 2z, 3\}$ respectively. This means that the $c^{(1)}$ correlation function can be uniquely expressed in terms of these coefficients and, consequently, eqn (A3) and (A4) form a closed set of equations in these coefficients. To solve these equations we use an iterative method with a mixing parameter of 0.5. The solution is obtained after typically 30 iterations, and starting values for the coefficients were chosen from the values obtained for a previous density.

Columnar phase

In this case the Euler-Lagrange equation reads

$$f(\mathbf{r}_\perp; l, h) = \frac{x(l, h) e^{\Delta c^{(1)}(\mathbf{r}_\perp; l, h)}}{\frac{1}{a_c} \int_{a_c} d\mathbf{r}_\perp e^{\Delta c^{(1)}(\mathbf{r}_\perp; l, h)}}, \quad (\text{A7})$$

where $a_c = a^2$ is the area of the unit cell of the square lattice, and a the lattice parameter, and $\Delta c^{(1)}(\mathbf{r}_\perp; l, h) = c^{(1)}(\mathbf{r}_\perp; l, h) - c_0^{(1)}(l, h)$. Expanding in a Fourier series,

$$f(\mathbf{r}_\perp; l, h) = \sum_{n, m=0}^\infty f_{nm}(l, h) \cos(qnx) \cos(qmy), \quad (\text{A8})$$

with $f_{00}(l, h) = 1$, and $q = 2\pi/a$. Multiplying eqn (A8) by cosine functions in x and y and integrating over the unit cell, we obtain:

$$f_{nm}(l, h) = \frac{4x(l, h)}{(1 + \delta_{n0})(1 + \delta_{m0})} \frac{\int_{a_c} d\mathbf{r}_\perp e^{\Delta c^{(1)}(\mathbf{r}_\perp; l, h)} \cos(qnx) \cos(qmy)}{\int_{a_c} d\mathbf{r}_\perp e^{\Delta c^{(1)}(\mathbf{r}_\perp; l, h)}}. \quad (\text{A9})$$

Using the definition

$$\Upsilon_{rs, uv}^{(nm)} \equiv \int_0^\infty dl l^u \int_0^\infty dh h^v f_{nm}(l, h) \Xi_r\left(\frac{nql}{2}\right) \Xi_s\left(\frac{mql}{2}\right), \quad (\text{A10})$$

with $r, s = 0, 1, \dots$, $u, v = 0, 1, \dots$, and $\Xi_0(x) = \cos x$, $\Xi_1(x) = \sin x/x$, eqn (A7) can be written as a transcendental set of equations in $\{\Upsilon_{rs, uv}^{(nm)}\}$, which form a closed set of equations because

the average densities can be written in terms of solely these coefficients,

$$n_x(\mathbf{r}_\perp) = \rho_0 \sum_{n, m=0}^\infty e_x^{(nm)} \cos(qnx) \cos(qmx), \quad (\text{A11})$$

with

$$e_x = \{\Upsilon_{00,00}, \Upsilon_{10,10}, \Upsilon_{01,10}, \Upsilon_{00,01}, \Upsilon_{01,11}, \Upsilon_{10,11}, \Upsilon_{11,20}, \Upsilon_{11,21}\}, \quad (\text{A12})$$

for $\alpha = \{0, 1x, 1y, 1z, 2x, 2y, 2z, 3\}$, respectively, and for each value of n, m . An iterative method was used to solve the equations with a mixing parameter of 0.5 and typically 100 iterations were necessary to reach convergence. Starting values for a given density were obtained from the solution of a previous density.

Appendix B: bifurcation analysis

In this section we give details on the bifurcation analysis from the N phase with respect to the S or C phases of the poly-disperse mixture. Eqn (12) can be rewritten as

$$\rho(\mathbf{r}; l, h) = \rho_0 x(l, h) e^{\Delta c^{(1)}(\mathbf{r}; l, h)}, \quad (\text{B1})$$

The nonuniform phase bifurcates from the parent phase and, near the bifurcation point, we can assume that $\rho(\mathbf{r}; l, h) \approx \rho_0 x(l, h) + \varepsilon(\mathbf{r}; l, h)$ where $\varepsilon(\mathbf{r}; l, h)$ is a small perturbation. Inserting this into eqn (B1) and functionally expanding the exponential up to first order in $\varepsilon(\mathbf{r}; l, h)$, we arrive at

$$\varepsilon(\mathbf{r}; l, h) = \rho_0 x(l, h) \int_0^\infty d\mathbf{l}' \int_0^\infty dh' \int d\mathbf{r}' c^{(2)}(\mathbf{r} - \mathbf{r}'; l, h, l', h') \varepsilon(\mathbf{r}'; l', h'). \quad (\text{B2})$$

with $c^{(2)}(\mathbf{r} - \mathbf{r}'; l, h, l', h')$ the direct correlation function:

$$c^{(2)}(\mathbf{r} - \mathbf{r}'; l, h, l', h') = \left. \frac{\delta c^{(1)}(\mathbf{r}; l, h)}{\delta \rho(\mathbf{r}', l', h')} \right|_{\rho(\mathbf{r}; l, h) = \rho_0 x(l, h)}. \quad (\text{B3})$$

In Fourier space, eqn (B2) becomes

$$\hat{\varepsilon}(\mathbf{q}; l, h) = \rho_0 x(l, h) \int_0^\infty d\mathbf{l}' \int_0^\infty dh' \hat{c}^{(2)}(\mathbf{q}; l, h, l', h') \hat{\varepsilon}(\mathbf{q}; l', h'). \quad (\text{B4})$$

where, as usual, $\hat{f}(\mathbf{q}) = \int d\mathbf{r} e^{i\mathbf{q}\cdot\mathbf{r}} f(\mathbf{r})$. The Fourier transform of the direct correlation function can be written as

$$-\hat{c}^{(2)}(\mathbf{q}; l, h, l', h') = \sum_{\alpha, \beta} \Phi_{\alpha\beta}(\rho_0) \hat{\omega}^{(\alpha)}(\mathbf{q}; l, h) \hat{\omega}^{(\beta)}(\mathbf{q}; l', h'). \quad (\text{B5})$$

where the coefficients $\Phi_{\alpha\beta} = \frac{\partial^2 \Phi}{\partial n_\alpha \partial n_\beta}$ are evaluated at $\rho(\mathbf{r}; l, h) = \rho_0 x(l, h)$. Therefore these coefficients are functions of ρ_0 and δ_l since, in the uniform limit, the weighted densities $n_x(\mathbf{r})$ are $n_0 = n_{1x} = n_{1y} = n_{1z} = n_{2x} = n_{2y} = \rho_0$ and $n_{2z} = n_3 = \rho_0(1 + \delta_l^2)$. $\hat{\omega}^{(\alpha)}(\mathbf{q}; l, h)$ are the Fourier transforms of the weights $\omega^{(\alpha)}(\mathbf{r}; l, h)$. Substitution of eqn (B5) into eqn (B4) gives

$$\hat{\varepsilon}(\mathbf{q}; l, h) = -\rho_0 x(l, h) \sum_{\alpha, \beta} \hat{\omega}^{(\alpha)}(\mathbf{q}; l, h) \Phi_{\alpha\beta}(\rho_0) s_\beta(\mathbf{q}), \quad (\text{B6})$$

where we have defined

$$s_\beta(\mathbf{q}) = \int_0^\infty dl \int_0^\infty dh \hat{\omega}^{(\beta)}(\mathbf{q}; l, h) \hat{\varepsilon}(\mathbf{q}; l, h). \quad (\text{B7})$$

Multiplying (B6) by $\hat{\omega}^{(\tau)}(\mathbf{q}; l, h)$ and integrating over l and h , we find

$$\mathbf{s}(\mathbf{q}) = -\rho_0 [\hat{T}(\mathbf{q}) \cdot \hat{\Phi}(\rho_0)] \mathbf{s}(\mathbf{q}), \quad (\text{B8})$$

where $\mathbf{s}(\mathbf{q})$ is a column vector of dimension eight with coordinates $s_\beta(\mathbf{q})$ ($\beta = 0, 2, 1x, 1y, 1z, 2z, 2y, 2z$), $\hat{\Phi}(\rho_0)$ is the matrix with elements $\Phi_{\alpha\beta}(\rho_0)$, and $\hat{T}(\mathbf{q})$ is the 8×8 matrix with elements

$$T_{\alpha\beta}(\mathbf{q}) = \int_0^\infty dl \int_0^\infty dh x(l, h) \hat{\omega}^{(\alpha)}(\mathbf{q}; l, h) \hat{\omega}^{(\beta)}(\mathbf{q}; l, h). \quad (\text{B9})$$

Defining the matrix

$$\hat{H}(\rho_0, \mathbf{q}) = I + \rho_0 \hat{T}(\mathbf{q}) \cdot \hat{\Phi}(\rho_0), \quad (\text{B10})$$

with I the 8×8 identity matrix, eqn (B8) can be rewritten as

$$\hat{H}(\rho_0, \mathbf{q}) \mathbf{s}(\mathbf{q}) = 0. \quad (\text{B11})$$

Thus, a nontrivial solution of (B11) can be calculated from

$$\mathcal{H}(\rho_0, \mathbf{q}) = 0, \quad \nabla_{\mathbf{q}} \mathcal{H}(\rho_0, \mathbf{q}) = 0, \quad (\text{B12})$$

i.e. by searching for the equality to zero of the global minimum of $\mathcal{H}(\rho_0, \mathbf{q}) = \det[\hat{H}(\rho_0, \mathbf{q})]$. The bifurcation to the S or C phases can be obtained using $\mathbf{q} = (0, 0, q)$ or $\mathbf{q} = (q, 0, 0)$, respectively, and the solutions of eqn (B12) furnish the values of density and wavevector, ρ_0^* and q^* , at bifurcation. Now taking into account the factorised form of the weighting functions,

$$\hat{\omega}^{(\alpha)}(\mathbf{q}; l, h) = \hat{\omega}_x^{(\alpha)}(q_x; l) \hat{\omega}_y^{(\alpha)}(q_y; l) \hat{\omega}_z^{(\alpha)}(q_z; h), \quad (\text{B13})$$

and of the parent size probability distribution $x(l, h) = \phi(l)\phi(h)$, the coefficients (B9) can be written as a product of two one-dimensional integrals:

$$T_{\alpha\beta}(\mathbf{q}) = \left[\int_0^\infty dl \phi(l) \prod_{\tau=\alpha, \beta} \hat{\omega}_x^{(\tau)}(q_x; l) \hat{\omega}_y^{(\tau)}(q_y; l) \right] \times \left[\int_0^\infty dh \phi(h) \prod_{\tau=\alpha, \beta} \hat{\omega}_z^{(\tau)}(q_z; h) \right]. \quad (\text{B14})$$

Finally, substituting the values $q_x = q_y = 0$, $q_z = q$ or $q_x = q$, $q_y = q_z = 0$ in these integrals, we find that they can be expressed as a function of the following integrals:

$$S_n(q) = \int_0^\infty d\sigma \phi(\sigma) \sigma^n \sin(q\sigma), \quad (\text{B15})$$

$$C_n(q) = \int_0^\infty d\sigma \phi(\sigma) \sigma^n \cos(q\sigma),$$

where $\sigma = \{l, h\}$. In turn, these integrals can efficiently be calculated as

$$S_n(q) = q \langle \sigma^{n+1} \rangle \exp\left(-\frac{q^2}{4\lambda}\right) M\left[-\frac{(\gamma+n-1)}{2}, \frac{3}{2}, \frac{q^2}{4\lambda}\right], \quad (\text{B16})$$

$$C_n(q) = \langle \sigma^n \rangle \exp\left(-\frac{q^2}{4\lambda}\right) M\left[-\frac{(\gamma+n)}{2}, \frac{1}{2}, \frac{q^2}{4\lambda}\right],$$

where $M[a, b, x]$ is the Confluent Hypergeometric function of real arguments (the so-called *Kummer function*³⁴), while the general expression for the n -th moment of the distribution function $\phi(\sigma)$ is

$$\langle \sigma^n \rangle = \frac{\Gamma\left[\frac{\gamma+n+1}{2}\right] \Gamma^{n-1}\left[\frac{\gamma+1}{2}\right]}{\Gamma^n\left[\frac{\gamma+2}{2}\right]}. \quad (\text{B17})$$

Acknowledgements

Financial support from Comunidad Autónoma de Madrid (Spain) under the R&D Programme of Activities MODELICO-CM/S2009ESP-1691, and from MINECO (Spain) under grants FIS2010-22047-C01 and FIS2010-22047-C04 is acknowledged.

References

- 1 F. M. van der Kooij, K. Kassapidou and H. N. W. Lekkerkerker, *Nature*, 2000, **406**, 868.
- 2 F. M. van der Kooij and H. N. W. Lekkerkerker, *Phys. Rev. Lett.*, 2000, **84**, 781.
- 3 J. G. Vroege, D. M. E. Thies-Weesie, A. V. Petukhov, B. J. Lemaire and P. Davidson, *Adv. Mater.*, 2006, **18**, 2565.
- 4 A. A. Verhoeff, H. H. Wensink, M. Vis, G. Jackson and H. N. W. Lekkerkerker, *J. Phys. Chem. B*, 2009, **113**, 13476.
- 5 A. B. G. M. Leferink op Reinink, E. van den Pol, D. V. Byelov, A. V. Petukhov and G. J. Vroege, *J. Phys.: Condens. Matter*, 2012, **24**, 464127.
- 6 F. M. van der Kooij, D. van der Beek and H. N. W. Lekkerkerker, *J. Phys. Chem. B*, 2001, **105**, 1696.
- 7 P. B. Warren, *Phys. Rev. Lett.*, 1997, **80**, 1369.
- 8 P. Sollich, *J. Phys.: Condens. Matter*, 2002, **14**, R79.
- 9 T. J. Sluckin, *Liq. Cryst.*, 1989, **6**, 111.
- 10 N. Clarke, J. A. Cuesta, R. Sear, P. Sollich and A. Speranza, *J. Chem. Phys.*, 2000, **113**, 5817.
- 11 A. Speranza and P. Sollich, *J. Chem. Phys.*, 2002, **117**, 5421.
- 12 P. Sollich, *J. Chem. Phys.*, 2005, **122**, 214911.
- 13 Y. Martínez-Ratón and J. A. Cuesta, *Phys. Rev. Lett.*, 2002, **89**, 185701.
- 14 Y. Martínez-Ratón and J. A. Cuesta, *J. Chem. Phys.*, 2003, **118**, 10164.
- 15 S. Belli, A. Patti, M. Dijkstra and R. van Roij, *Phys. Rev. Lett.*, 2011, **107**, 148303.
- 16 M. A. Bates and D. Frenkel, *J. Chem. Phys.*, 1999, **110**, 6553.
- 17 M. A. Bates and D. Frenkel, *J. Chem. Phys.*, 1998, **109**, 6193.
- 18 D. Sun, H.-J. Sue, Z. Cheng, Y. Martínez-Ratón and E. Velasco, *Phys. Rev. E*, 2009, **80**, 041704.
- 19 A. F. Mejia, Y.-W. Chang, R. Ng, M. Shuai, M. S. Mannan and Z. Cheng, *Phys. Rev. E*, 2012, **85**, 061708.
- 20 Y. Martínez-Ratón and E. Velasco, *J. Chem. Phys.*, 2011, **134**, 124904.
- 21 Y. Martínez-Ratón and E. Velasco, *J. Chem. Phys.*, 2012, **137**, 134906.

- 22 B. S. John, C. Juhlin and F. A. Escobedo, *J. Chem. Phys.*, 2008, **128**, 044909.
- 23 M. R. Wilson, P. D. Duncan, M. Dennison and A. J. Masters, *Soft Matter*, 2012, **8**, 3348.
- 24 J. A. Cuesta and Y. Martínez-Ratón, *J. Chem. Phys.*, 1997, **107**, 6379.
- 25 Y. Martínez-Ratón and J. A. Cuesta, *J. Chem. Phys.*, 1999, **111**, 317.
- 26 D. de las Heras and M. Schmidt, *Soft Matter*, 2013, **9**, 8636.
- 27 Y. Martínez-Ratón, *Phys. Rev. E*, 2004, **69**, 061712.
- 28 S. Belli, M. Dijkstra and R. van Roij, *J. Chem. Phys.*, 2012, **137**, 124506.
- 29 E. van den Pol, D. M. E. Thies-Weesie, A. V. Petukhov, G. J. Vroege and K. Kvashina, *J. Chem. Phys.*, 2008, **129**, 164715.
- 30 A. V. Petukhov, D. van der Beek, R. P. A. Dullens, I. P. Dolbnya, G. J. Vroege and H. N. W. Lekkerkerker, *Phys. Rev. Lett.*, 2005, **95**, 077801.
- 31 D. van der Beek, A. V. Petukhov, S. M. Oversteegen, G. J. Vroege and H. N. W. Lekkerkerker, *Eur. Phys. J. E: Soft Matter Biol. Phys.*, 2005, **16**, 253.
- 32 D. M. E. Thies-Weesie, J.-P. de Hoog, M. H. Hernandez-Mendiola, A. V. Petukhov and G. J. Vroege, *Chem. Mater.*, 2007, **19**, 5538.
- 33 D. Kleshchanok, P. Holmqvist, J.-M. Meijer and H. N. W. Lekkerkerker, *J. Am. Chem. Soc.*, 2012, **134**, 5985.
- 34 I. S. Gradshteyn and L. M. Ryzhik, in *Table of integrals series and products*, ed. A. Jeffrey and D. Zwillinger, Academic Press, 7th edn, 2007.